Physics of Fluids

Phase-field modeling of selective laser brazing of diamond grits

Cite as: Phys. Fluids **33**, 052113 (2021); https://doi.org/10.1063/5.0049096
Submitted: 01 March 2021 . Accepted: 17 April 2021 . Published Online: 14 May 2021

Lu Li (李露), Shuai Li (李帅), Bi Zhang (张璧), and Tai-Hsi Fan (范代禧)

Physics of Fluids ARTICLE scitation.org/journal/phf

Phase-field modeling of selective laser brazing of diamond grits

Cite as: Phys. Fluids 33, 052113 (2021); doi: 10.1063/5.0049096
Submitted: 1 March 2021 · Accepted: 17 April 2021 ·
Published Online: 14 May 2021

Lu Li (李露),[1] Shuai Li (李帅),[2] Bi Zhang (张璧),[1,2] and Tai-Hsi Fan (范代禧)[1,a)]

AFFILIATIONS

[1]Department of Mechanical Engineering, University of Connecticut, Storrs, Connecticut 06269, USA
[2]Department of Mechanical and Energy Engineering, Southern University of Science and Technology, Shenzhen 518055, China

[a)]Author to whom correspondence should be addressed: thfan05@gmail.com

ABSTRACT

Diamond grit is widely used in cutting, grinding, and polishing tools for its superior mechanical properties and performance in machining hard materials. Selective laser brazing (SLB) of diamond grits is a new additive manufacturing technique that has great potential to fabricate the next generation of high-performance diamond tools. However, fundamental understanding and quantitative analysis for the design and tuning of the SLB process and the resulting bonding efficiency are not yet established as the process is complicated by heating, fusion, wetting, solidification, grit migration, bonding, reaction, and the interplay between these effects. We present a thermodynamically consistent phase-field theoretical model for the prediction of melting and wetting of SLB on diamond grits using a powder-based additive manufacturing technique. The melting dynamics is driven by laser heating in a chamber filled with argon gas and is coupled with the motion of multiple three-phase contact lines. The relevant wetting dynamics, interfacial morphology, and temperature distribution are computationally resolved in a simplified two-dimensional (2D) configuration.

I. INTRODUCTION

Synthetic diamond tools have long been developed for a variety of applications in machining metallic, glass, ceramic, and composite materials.[1–6] Having advantages of superior hardness, tensile strength, thermal conductivity, wear resistance, self-sharpening capability, and low friction and low thermal expansion coefficient, synthetic diamond grits in a metal matrix are often used in producing cutting, grinding, and polishing tools for the machining of hard materials.[7–9] Two types of brazing filler metals are widely used in brazing diamond tools, that is, copper-based medium-temperature alloys and nickel-based high-temperature materials.[10–15] The former has a relatively low operating temperature and thus lower risk of graphitization and cracks due to mild residual stress; however, it suffers from lower mechanical strength and less wear resistance. The latter has a strong affinity to diamond, great chemical resistance, and wearing resistance; however, nickel could catalyze the graphitization of diamond grits at high temperature. In practices, phosphorus, boron, and carbon are often alloyed with nickel to reduce the melting temperature and alleviate the graphitization problem. Chromium can also be added as an active metal to form carbide, which enhances the bonding of diamond grits to the substrate.

The performance and service life of diamond tools are often limited by the pullout of grits during operation, which is associated with the impregnated depth of diamond grits in the metal filler as well as the wetting profile, protrusion height from the filler metal, and the cutting conditions. Electroplating and brazing are two major techniques in fabricating surface-set diamond tools. In electroplating, diamond grits are evenly covered by the plating metal as mechanical support; however, the bonding force is relatively weak as a recess cavity region often appears in the brazing material around each grit and cannot guarantee the performance of the diamond tool for an aggressive cutting at the higher speed.[16,17] In the selective laser brazing (SLB) process, the filler metal is melted by heating first, providing wetting effectively to the substrate and diamond grits. As the grits are firmly embedded in the brazing alloy, higher bonding force and thus better tool life and performance are expected than those electroplated diamond tools.[17]

Because brazing dynamics is complicated by heating, fusion, wetting, solidification, and chemical reaction,[18] the local heat transfer rate and temperature distribution would significantly affect the formation of the intermetallic phase and residual stress.[19] Therefore, careful control and optimization of the process are essential to the success of

making brazing diamond tools. With the recent advancement of additive manufacturing of metallic parts, fabrication of metal-diamond composite is further developed by using selective laser melting (SLM) and laser cladding process.[20,21] Selective laser brazing (SLB) of diamond grits is an additive manufacturing technique that holds promise for adjusting the temperature, degree of melting of the filler metal, brazing profile, protrusion height of the diamond grits, and to improve bonding or adhesion force, yet reducing the risk of graphitization and microcracks. Selective laser brazing would have advantages on better control of the spatial arrangement of diamond grits and microstructure of the metal composite matrix. However, there exist no details about transient brazing dynamics and predictive modeling tools that can facilitate basic understanding and rapid design of the process.

In this article, we focus on the first approximation of the phase transition and 2D wetting dynamics during the SLB process with an assumed fixed diamond-grit configuration. As wetting dynamics is essential for a firm bonding between diamond grits and the substrate, reaction and formation of the intermetallic phase are neglected to simplify the model. The diffuse interface or phase-field method[22–27] is applied to the derivation of phase transition and transport equations in the proposed theoretical framework. The phase-field approach has the advantage of describing transient and multiphase dynamics without explicitly tracking the moving boundaries. The details of wetting dynamics are described by the multicomponent Cahn–Hilliard type equation, whereas the Allen-Cahn equation is used for solid–liquid phase transition of the filler metal. The phase-field method has been developed primarily for investigating the growth kinetics, interfacial patterning, and the stability of dendritic microstructure in metallic systems.[28–33] The phase field method can also include other effects, such as elastic energy, electrical field, magnetic field, and thermofluid dynamics.[34–45] Recently, we have extended the phase-field approach and thermal-fluid analysis to the applications in additive manufacturing[46,47] and biopharmaceutical processing.[48,49] In the SLB additive manufacturing process, the contact line dynamics can be described by an order parameter (phase-field variable) with interfacial boundary conditions obtained from either surface energy,[50] geometrical contact angle,[51–53] or imposed constraint to minimize the resulting free energy.[54–56] Here, we adopt the constraint approach for its completeness in describing the evolution of contact lines and the transient wetting dynamics.

II. THEORETICAL ANALYSIS

Figure 1 shows the simplified setting of our model system with diamond grits and powders made of the filler metal, presumed alternately placed on top of the coated substrate. Upon laser heating and melting of the filler metal, wetting and spreading introduce interfacial motion and fluid flow around the diamond grits. The subsequent solidification immerses the grits and provides bonding of the grits to the substrate surface. The following assumptions are made to facilitate the theoretical analysis: (i) the diamond grits are assumed fixed to the same location; that is, the motion or migration of grits is neglected; (ii) characteristic size of the Gaussian laser beam is assumed of the same order of magnitude as grits and powders; (iii) evaporation and condensation of the filler metal are neglected; (iv) chemical reaction and intermetallic phase formation are not included; (v) the latent heat, heat capacity, density, and dynamic viscosity of the filler metal are assumed constant, whereas the thermal conductivity is temperature dependent; (vi) thermal Marangoni effect along the liquid–gas interface is neglected; (vii) the nominal size of the powders is about the same as diamond grits with a periodic spatial arrangement; and (viii) the ambient argon gas is assumed ideal.

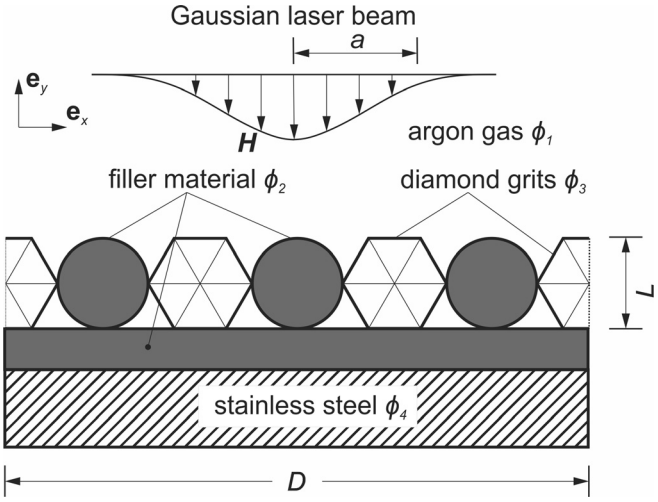

FIG. 1. Schematic of selective laser brazing (SLB) process on a tool surface. A stainless steel substrate is coated with the filler metal, and diamond grits are affixed on top of it. Melting of the powders made of the same filler metal between grits provides bonding of grits to the substrate. ϕ_1 to ϕ_4 are the corresponding material volume fractions. Length L is the characteristic size of grits with an assumed hexagonal shape, D represents the width of the computational domain with periodic configuration, and the Gaussian beam is featured by an irradiation intensity $\boldsymbol{H}$ and characteristic spot radius a.

A. Entropy functional

Following the thermodynamically consistent phase-field approach,[24,25,27] we express the entropy functional of the system as

$$\mathcal{S}' = \int_\Omega \mathcal{L}' dV = \int_\Omega \left[s(e, \varphi, \phi_1, \phi_2, \phi_3, \phi_4) - \frac{1}{2}\xi_\varphi^2 |\nabla\varphi|^2 - \frac{1}{2}\sum_{i=1}^{4} \xi_i^2 |\nabla\phi_i|^2 \right] dV, \quad (1)$$

where Ω indicates the physical and computational domain, including the substrate, filler metal, diamond grits, and the argon gas environment; the integrand $\mathcal{L}'$ of the entropy functional includes the contributions of gradient entropy effect across the interfaces and the local entropy s (per unit volume) within the bulk phase as a function of the internal energy e, solid–liquid phase-field variable φ, and volume fractions of the argon gas ϕ_1, filler metal ϕ_2, diamond ϕ_3, and substrate ϕ_4. The assumed constant gradient coefficients ξ_φ and $\xi_{1\sim4}$ associated with the corresponding gradient effects are connected with the interfacial energy, thickness, and the constraint to the three-phase contact line. The phase-field variable $\varphi \in [-1, 1]$ (−1 for the liquid phase and +1 for the solid phase) is a non-conserved order parameter to describe solid–liquid phase change, whereas ϕ_1 to $\phi_4 \in [0, 1]$ are material volume fractions as conserved phase-field variables under a constraint of $\sum_{i=1}^{4} \phi_i = 1$. The entropy functional $\mathcal{S}'$ can be modified and written as a constrained form:

$$\mathcal{S} = \int_\Omega \mathcal{L} dV = \int_\Omega \left[s - \lambda \left(\sum_{i=1}^{4} \phi_i - 1 \right) - \frac{1}{2} \xi_\varphi^2 |\nabla \varphi|^2 - \frac{1}{2} \sum_{i=1}^{4} \xi_i^2 |\nabla \phi_i|^2 \right] dV \,, \tag{2}$$

where λ is a Lagrange multiplier to be determined, and $\mathcal{L}$ is the revised integrand that incorporates the constraint. Now, we consider the time derivative of the above entropy functional,

$$\frac{d\mathcal{S}}{dt} = \int_\Omega \left(\frac{\partial s}{\partial e}\frac{\partial e}{\partial t} + \frac{\partial s}{\partial \varphi}\frac{\partial \varphi}{\partial t} + \sum_{i=1}^{4} \frac{\partial s}{\partial \phi_i}\frac{\partial \phi_i}{\partial t} + \frac{\partial \mathcal{L}}{\partial \nabla \varphi} \nabla \frac{\partial \varphi}{\partial t} + \sum_{i=1}^{4} \frac{\partial \mathcal{L}}{\partial \nabla \phi_i} \nabla \frac{\partial \phi_i}{\partial t} \right) dV \,, \tag{3}$$

which can be arranged to an Euler–Lagrange form as

$$\frac{d\mathcal{S}}{dt} = \int_\Omega \left[\frac{\partial s}{\partial e}\frac{\partial e}{\partial t} + \left(\frac{\partial s}{\partial \varphi} - \nabla \cdot \frac{\partial \mathcal{L}}{\partial \nabla \varphi} \right) \frac{\partial \varphi}{\partial t} + \sum_{i=1}^{4} \left(\frac{\partial s}{\partial \phi_i} - \nabla \cdot \frac{\partial \mathcal{L}}{\partial \nabla \phi_i} \right) \times \frac{\partial \phi_i}{\partial t} + \nabla \cdot \left(\frac{\partial \varphi}{\partial t}\frac{\partial \mathcal{L}}{\partial \nabla \varphi} + \sum_{i=1}^{4} \frac{\partial \phi_i}{\partial t}\frac{\partial \mathcal{L}}{\partial \nabla \phi_i} \right) \right] dV \,. \tag{4}$$

By using variational operator δ, Eq. (4) can be expressed as

$$\frac{d\mathcal{S}}{dt} = \int_\Omega \left[\frac{\delta \mathcal{S}}{\delta e}\frac{\partial e}{\partial t} + \frac{\delta \mathcal{S}}{\delta \varphi}\frac{\partial \varphi}{\partial t} + \sum_{i=1}^{4} \frac{\delta \mathcal{S}}{\delta \phi_i}\frac{\partial \phi_i}{\partial t} + \nabla \cdot \left(\frac{\partial \varphi}{\partial t}\frac{\partial \mathcal{L}}{\partial \nabla \varphi} + \sum_{i=1}^{4} \frac{\partial \phi_i}{\partial t}\frac{\partial \mathcal{L}}{\partial \nabla \phi_i} \right) \right] dV \,, \tag{5}$$

where the first variation of the entropy functional with respect to the internal energy e, phase field φ, and volume fraction ϕ_i are

$$\frac{\delta \mathcal{S}}{\delta e} = \frac{\partial s}{\partial e} = \frac{1}{T} \,, \tag{6}$$

$$\frac{\delta \mathcal{S}}{\delta \varphi} = \frac{\partial s}{\partial \varphi} - \nabla \cdot \frac{\partial \mathcal{L}}{\partial \nabla \varphi} = \frac{\partial s}{\partial \varphi} + \xi_\varphi^2 \nabla^2 \varphi \,, \tag{7}$$

and

$$\frac{\delta \mathcal{S}}{\delta \phi_i} = \frac{\partial s}{\partial \phi_i} - \nabla \cdot \frac{\partial \mathcal{L}}{\partial \nabla \phi_i} = \frac{\partial s}{\partial \phi_i} + \xi_i^2 \nabla^2 \phi_i, \tag{8}$$

respectively, where T is temperature and $i = 1$–4.

Furthermore, based on the entropy transport equation, the time derivative of the entropy functional can be written as

$$\frac{d\mathcal{S}}{dt} = \int_\Omega \left[\nabla \cdot (-\boldsymbol{J}_s) + \dot{\Gamma} + \frac{\dot{Q}}{T} \right] dV \,, \tag{9}$$

where $\boldsymbol{J}_s$ represents entropy flux; $\dot{\Gamma}$ is local entropy generation rate, which has a positive value according to the 2nd law of thermodynamics; and $\dot{Q}$ accounts for the heat source ($\dot{Q} > 0$) or sink ($\dot{Q} < 0$) effect. By combining Eqs. (5) and (9) and with integration over an arbitrary material domain, the differential entropy transport equation leads to

$$\nabla \cdot (-\boldsymbol{J}_s) + \dot{\Gamma} + \frac{\dot{Q}}{T} = \frac{\delta \mathcal{S}}{\delta e}\frac{\partial e}{\partial t} + \sum_{i=1}^{4} \frac{\delta \mathcal{S}}{\delta \phi_i}\frac{\partial \phi_i}{\partial t} + \frac{\delta \mathcal{S}}{\delta \varphi}\frac{\partial \varphi}{\partial t} + \nabla \cdot \left(\frac{\partial \varphi}{\partial t}\frac{\partial \mathcal{L}}{\partial \nabla \varphi} + \sum_{i=1}^{4} \frac{\partial \phi_i}{\partial t}\frac{\partial \mathcal{L}}{\partial \nabla \phi_i} \right), \tag{10}$$

which forms the basis of governing transport equations and the evolution of phase-field variables that describe the laser brazing problem in hand.

B. Energy equation

The differential energy equation in terms of the variational derivative of $\mathcal{S}$ can be expressed as

$$\frac{\partial e}{\partial t} + \boldsymbol{v} \cdot \nabla e = -\nabla \cdot \left(M_e \nabla \frac{\delta \mathcal{S}}{\delta e} \right) + \Phi + \dot{Q} \,, \tag{11}$$

and by selecting the mobility coefficient $M_e = k_T T^2$ as a function of the temperature-dependent thermal conductivity k_T, the first term on the right-hand side reduces to the classical Fourier heat conduction effect. The viscous dissipation function $\Phi = \boldsymbol{\sigma}_{\text{vis}} : \nabla \boldsymbol{v}$ is for an assumed Newtonian fluid, with $\boldsymbol{\sigma}_{\text{vis}}$ and $\boldsymbol{v}$ representing the fluid flow viscous stress and the velocity field, respectively. The heat source term $\dot{Q}$ incorporates the radiation lose $\dot{Q}_r$ and laser irradiation $\dot{Q}_{ir}$ effects to be defined later on. Note that the local and convective derivatives on the left-hand side can be replaced by the substantial derivative of the internal energy, De/Dt.

The additive internal energy is given by $e = \sum_{i=1}^{4} \phi_i e_i$, where e_1, e_3, and e_4 are the internal energy of pure argon gas, diamond, and substrate, respectively, whereas e_2 is the internal energy of the filler metal that follows:

$$e_2(T, \varphi) = e_2^{(s)}(T) + P(\varphi) L_a \,, \tag{12}$$

where $e_2^{(s)}$ indicates internal energy density (per unit volume) of the solid phase of the filler metal, L_a is an assumed constant latent heat of melting for the filler metal, and $P(\varphi)$ is an interpolation function across solid and liquid phases, here defined as

$$P(\varphi) = 1/2 - 1/16\left(3\varphi^5 - 10\varphi^3 + 15\varphi\right). \tag{13}$$

The above polynomial function satisfies $P' = P'' = 0$ at $\varphi = \pm 1$,[25] so that $P(1) = 0$ indicates the solid phase and $P(-1) = 1$ for the liquid phase. By incorporating the latent heat effect into the phase-field approach, the time derivative of internal energy can be approximated by

$$\frac{De}{Dt} \simeq \sum_{i=1}^{4} \phi_i \frac{De_i}{Dt} = \phi_2 P' L_a \frac{D\varphi}{Dt} + \sum_{i=1}^{4} \left(\phi_i \rho_i c_{p_i} \frac{DT}{Dt} \right). \tag{14}$$

We further assume that all specific heats, denoted by c_{p_i}, are temperature-independent, and for the solid and liquid phases of the filler metal, we have $c_{p_2}^{(s)} \simeq c_{p_2}^{(\ell)} = c_{p_2}$. As a result, the energy equation (11) can be written as

$$\sum_{i=1}^{4} \phi_i \rho_i c_{p_i} \frac{DT}{Dt} = \nabla \cdot (k_T \nabla T) + \boldsymbol{\sigma}_{\text{vis}} : \nabla \boldsymbol{v} + \dot{Q}_r + \dot{Q}_{ir} - \phi_2 P' L_a \frac{D\varphi}{Dt} \,, \tag{15}$$

where temperature-dependent thermal conductivity k_T has covered the contribution from each phase and can be calculated by

$$k_T = \sum_{i=1}^{4} \phi_i k_{T_i}\,, \tag{16}$$

with k_{T_1} to k_{T_4} indicating the temperature-dependent thermal conductivity for argon, filler metal, diamond grits, and the substrate, respectively. The radiation heat loss to the environment and irradiation of the laser beam at the surface ($\partial\Omega$) of the diamond grits and filler metal are calculated by

$$\dot{Q}_r(\mathbf{x} \in \partial\Omega) = -\frac{\epsilon\sigma_B(T^4 - T_a^4)}{W} \tag{17}$$

and

$$\dot{Q}_{ir}(\mathbf{x} \in \partial\Omega) = -\frac{\alpha \boldsymbol{H}\cdot\boldsymbol{n}}{W}\,, \tag{18}$$

respectively, where $\epsilon = \sum_{i=2}^{4} \phi_i\epsilon_i$ is the emissivity of the surface with apparent characteristic width W, ϵ_i represents emissivity of each corresponding phase, σ_B is the Stefan–Boltzmann constant, T_a is the ambient temperature, α is the absorptivity of the system assumed approximately the same as ϵ, $\boldsymbol{n}$ is the outward surface normal pointing from the filler metal or diamond grits to the ambient gas environment, determined by $\boldsymbol{n} = \nabla\phi_1/|\nabla\phi_1|$, and $\boldsymbol{H}$ is the intensity of an assumed 2D Gaussian laser beam. Note that gas participation in thermal radiation is neglected here. The heat flux of the Gaussian laser beam can be approximated by

$$\boldsymbol{H} = \frac{-\sqrt{2/\pi}\mathcal{Q}}{a}\exp\left[\frac{-2(x - x_0 - U_a t)^2}{a^2}\right]\hat{\mathbf{e}}_y\,, \tag{19}$$

where $\mathcal{Q}$ is the laser power per unit length, a is the characteristic spot radius, x is horizontal coordinate, x_0 is the initial position, and U_a is the scanning speed of the laser beam traveling along the horizontal direction ($\hat{\mathbf{e}}_x$, Fig. 1). Note that the heat flux for a uniform laser beam in the test case is approximated by $\boldsymbol{H}_u = -(\mathcal{Q}/D)\,\hat{\mathbf{e}}_y$.

C. Phase-field evolution equations

Following the entropy transport equation [Eq. (10)] and with a positive entropy generation rate $\dot{\Gamma}$, the time evolution of the non-equilibrium solid–liquid phase field φ is assumed linearly proportional to the entropy driving force $\delta\mathcal{S}/\delta\varphi$, written as

$$\frac{\partial\varphi}{\partial t} = M_\varphi\frac{\delta\mathcal{S}}{\delta\varphi} = M_\varphi\left(\frac{\partial s}{\partial\varphi} + \xi_\varphi^2\nabla^2\varphi\right), \tag{20}$$

where the assumed positive proportional constant, M_φ, is the so-called interfacial mobility, and the first variation of entropy functional comes from Eq. (7). Furthermore, the transient evolution of each volume fraction ϕ_i as a conserved phase-field variable follows the Cahn–Hilliard type evolution equation,[22] expressed as

$$\frac{\partial\phi_i}{\partial t} = -\nabla\cdot\left[M_i\nabla\left(\frac{\delta\mathcal{S}}{\delta\phi_i}\right)\right] = -\nabla\cdot\left[M_i\nabla\left(\frac{\partial s}{\partial\phi_i} + \xi_i^2\nabla^2\phi_i\right)\right], \tag{21}$$

for $i = 1$ to 4, where the positive mobility coefficients M_1 to M_4 are for argon gas, filler metal, diamond grits, and the substrate, respectively. As mixing is avoided across the boundaries of each component in this case, the mobility coefficients are no longer associated with Fickian-type species diffusivity. Here, the coefficients are determined by scaling analysis based on the comparison of characteristic time scales.

Now to associate $\partial s/\partial\varphi$ and $\partial s/\partial\phi_i$ in Eqs. (20) and (21) with internal energy and free energy density, the total derivative of internal energy $e(s, \varphi, \phi_1, \phi_2, \phi_3, \phi_4)$ is expressed as

$$de = Tds + \frac{\partial e}{\partial\varphi}d\varphi + \sum_{i=1}^{4}\frac{\partial e}{\partial\phi_i}d\phi_i\,, \tag{22}$$

and thus,

$$ds = \frac{1}{T}de - \frac{1}{T}\frac{\partial e}{\partial\varphi}d\varphi - \frac{1}{T}\sum_{i=1}^{4}\frac{\partial e}{\partial\phi_i}d\phi_i\,. \tag{23}$$

By comparing the partial derivatives of entropy $s(e, \varphi, \phi_1, \phi_2, \phi_3, \phi_4)$ with the above expression, one can establish the following relations:

$$\left.\frac{\partial s}{\partial\varphi}\right|_{e,\phi_1,\phi_2,\phi_3,\phi_4} = -\frac{1}{T}\left.\frac{\partial e}{\partial\varphi}\right|_{s,\phi_1,\phi_2,\phi_3,\phi_4}, \tag{24}$$

and

$$\left.\frac{\partial s}{\partial\phi_i}\right|_{e,\varphi,\phi_{j(j\neq i)}} = -\frac{1}{T}\left.\frac{\partial e}{\partial\phi_i}\right|_{s,\varphi,\phi_{j(j\neq i)}}, \tag{25}$$

for $i = 1$–4. Moreover, since the Helmholtz free energy density is introduced as $f(T, \varphi, \phi_1, \phi_2, \phi_3, \phi_4) = e - Ts$, the total derivative of free energy is

$$df = d(e - Ts) = -sdT + \frac{\partial e}{\partial\varphi}d\varphi + \sum_{i=1}^{4}\frac{\partial e}{\partial\phi_i}d\phi_i\,, \tag{26}$$

therefore,

$$\left.\frac{\partial e}{\partial\varphi}\right|_{s,\phi_1,\phi_2,\phi_3,\phi_4} = \left.\frac{\partial f}{\partial\varphi}\right|_{T,\phi_1,\phi_2,\phi_3,\phi_4}, \tag{27}$$

and

$$\left.\frac{\partial e}{\partial\phi_i}\right|_{s,\varphi,\phi_{j(j\neq i)}} = \left.\frac{\partial f}{\partial\phi_i}\right|_{T,\varphi,\phi_{j(j\neq i)}}, \tag{28}$$

for $i = 1$–4. By further incorporating the constraint of volume fraction and the Lagrange multiplier, the free energy density that is complementary to the bulk entropy density appeared in Eq. (2) can be formulated as

$$f = \sum_{i=1}^{4}\phi_i f_i + f_{\text{mix}} + T\lambda\left(\sum_{i=1}^{4}\phi_i - 1\right), \tag{29}$$

where the free energy density f_2 is for the filler metal, including both solid and liquid phases with an equilibrium free energy profile determined by a double-well potential,[25] written as

$$f_2 = T\left[-\int_{T_m}^{T}\frac{e_2(T', \varphi)}{T'^2}dT' + \frac{1}{4}h_\varphi\left(1 - \varphi^2\right)^2\right], \tag{30}$$

where T_m is the equilibrium melting temperature of the filler metal, internal energy e_2 is defined in Eq. (12), and h_φ is the corresponding

energy barrier (per degree Kelvin) across solid and liquid phases of the filler metal. Additional energy terms f_1, f_3, and f_4 are the free energy densities of pure argon, diamond, and the substrate, respectively. To avoid mixing of different components, here we introduce mixing free energy f_{mix} using a double-well type potential to accommodate the enthalpy effect:[49]

$$f_{\text{mix}} = T\sum_{i=1}^{4}\left[h_i\phi_i^2(1-\phi_i)^2\right], \tag{31}$$

where h_1 to h_4 are the energy barriers for mixing different components. The last term on the right-hand side of Eq. (29) takes Lagrange multiplier into account for the constraint $\sum_{i=1}^{4}\phi_i = 1$.

Now by combining the thermodynamic relationships above, the φ-derivative of entropy is approximated as

$$\frac{\partial s}{\partial \varphi} \simeq \phi_2\left[P'L_a\frac{T-T_m}{TT_m} + h_\varphi\left(\varphi-\varphi^3\right)\right], \tag{32}$$

where the latent heat is assumed temperature independent, and the ϕ_i-derivative is approximated as

$$\begin{aligned}\frac{\partial s}{\partial \phi_i} &\simeq -\frac{1}{T}\frac{\partial f_{\text{mix}}}{\partial \phi_i} - \lambda \\ &= -2h_i\phi_i(1-\phi_i)(1-2\phi_i) - \lambda,\end{aligned} \tag{33}$$

where the mixing enthalpy effect dominates the free energy expression. Finally, substituting Eq. (32) into Eq. (20), the φ-equation for solid–liquid phase transition becomes

$$\frac{\partial \varphi}{\partial t} = M_\varphi\left[\xi_\varphi^2\nabla^2\varphi + \phi_2P'L_a\frac{T-T_m}{TT_m} + \phi_2h_\varphi\left(\varphi-\varphi^3\right)\right], \tag{34}$$

where the evolution of the phase field φ is determined by three effects: the 2nd term on the right is the thermal driving force for solid–liquid phase transition by taking elevated temperature and latent heat into account, whereas 1st and 3rd terms indicate the balance of diffusive and double-well type phase separation effects for generating and evolving a smooth yet narrow interfacial profile. Similarly, substituting Eq. (33) to Eq. (21), the volume fraction phase-field equation can be formulated as

$$\frac{\partial \phi_i}{\partial t} = \nabla\cdot\left\{M_i\nabla\left[2h_i\phi_i(1-\phi_i)(1-2\phi_i) + \lambda - \xi_i^2\nabla^2\phi_i\right]\right\}, \tag{35}$$

for $i = 1$–4 in general. The double-well term prevents the mixing of different components, the Lagrange multiplier accounts for the constraint, and the 4th-order term takes the long-ranged effect into account, which is obtained originally from the entropy gradients. In the above phase-field evolution equations, the gradient coefficients ξ_φ^2 and ξ_i^2, and the energy barriers h_φ and h_i are associated with interfacial energy and characteristic thickness of the interface, which will be explained in Sec. II D. Note that to accommodate the fluid flow convective effect, hereafter we replace $\partial/\partial t$ by the substantial derivative $D/Dt \equiv \partial/\partial t + \boldsymbol{v}\cdot\nabla$, where $\boldsymbol{v}$ is the velocity field.

D. Interfacial energy and Lagrange multiplier

The interfacial energy γ is associated with the excess energy due to the appearance of the interface at equilibrium and can be estimated by the one-dimensional (1D) approximation of the phase-field profile.[22] As a result, the interfacial energy at the solid–liquid interface of the filler metal can be expressed as

$$\gamma_\varphi = \int_{-\infty}^{\infty}\left[T_m\xi_\varphi^2|\nabla\varphi|^2\right]dx = \frac{2\sqrt{2}}{3}\frac{\xi_\varphi^2}{W_\varphi}T_m, \tag{36}$$

where x indicates the coordinate in an assumed unbounded 1D domain, T_m is the reference temperature at the melting point of the filler metal, and W_φ is the characteristic thickness of interface correlated with the entropy gradient coefficient through $\xi_\varphi^2 = h_\varphi W_\varphi^2$. Similarly, the interfacial energy across two different components can be formulated by the general form:

$$\gamma_{ij} = \int_{-\infty}^{\infty}\left[T_{ij}^0\left(\xi_i^2+\xi_j^2\right)|\nabla\phi_i|^2\right]dx, \tag{37}$$

where i and j indicate the corresponding component, and T_{ij}^0 is the reference temperature. Considering $\phi_i \in [0,1]$, the interfacial energy between the filler metal and argon gas environment becomes

$$\gamma_{12} = \frac{\sqrt{2}}{6}\frac{\left(\xi_1^2+\xi_2^2\right)}{W_{12}}T_{12}^0 = \frac{\sqrt{2}}{6}(h_1+h_2)W_{12}T_{12}^0, \tag{38}$$

where W_{12} is the characteristic thickness of the interface between argon and filler metal. Similar expressions are applied to the interfacial energy between argon and diamond grits (γ_{13}), argon and stainless steel (γ_{14}), and the filler metal and diamond grits (γ_{23}). We further assign all reference temperatures to the melting point of filler metal, $T_{ij}^0 = T_m$, and apply the same characteristic thickness by letting $W_{ij} = W$. Further arrangement of the four entropy gradient coefficients for their corresponding components can be formulated by the interfacial energies as

$$\begin{bmatrix}\xi_1^2\\ \xi_2^2\\ \xi_3^2\\ \xi_4^2\end{bmatrix} = \frac{3W}{\sqrt{2}T_m}\begin{bmatrix}1 & 1 & -1 & 0\\ 1 & -1 & 1 & 0\\ -1 & 1 & 1 & 0\\ -1 & -1 & 1 & 2\end{bmatrix}\begin{bmatrix}\gamma_{12}\\ \gamma_{13}\\ \gamma_{23}\\ \gamma_{14}\end{bmatrix}. \tag{39}$$

In the multicomponent system, the energy barriers are further associated with the gradient coefficients and interfacial thickness as

$$h_i + h_j = \frac{\xi_i^2+\xi_j^2}{W^2}. \tag{40}$$

A reduction of the relationships leads to a decoupled form:

$$h_i = \frac{\xi_i^2}{W^2} \tag{41}$$

for $i = 1$–4.

Finally, following the derivation of Boyer *et al.*,[54,55] the Lagrange multiplier λ can be determined by combining Eqs. (21) and (33) and substituting into the constrain $\sum_{i=1}^{4}\phi_i = 1$, and then taking the time derivative of the constraint at an arbitrary temperature as

$$\begin{aligned}\frac{D}{Dt}\left(\sum_{i=1}^{4}\phi_i\right) = 0 = \nabla^2\left[\frac{1}{T}\sum_{i=1}^{4}\left(M_i\frac{\partial f_{\text{mix}}}{\partial\phi_i}\right) + \lambda\left(\sum_{i=1}^{4}M_i\right)\right. \\ \left. - \sum_{i=1}^{4}\left(M_i\xi_i^2\nabla^2\phi_i\right)\right].\end{aligned} \tag{42}$$

A simplified relationship was postulated by Boyer *et al.*[54,55] by letting

$$M_1\xi_1^2 = M_2\xi_2^2 = M_3\xi_3^2 = M_4\xi_4^2 = M_0, \tag{43}$$

where M_0 is a constant. The last term on the right-hand side of Eq. (42) vanishes due to the constraint, so that the resulting Lagrange multiplier becomes

$$\lambda = \frac{-1}{T\sum_{i=1}^{4} M_i}\left(\sum_{i=1}^{4} M_i \frac{\partial f_{\text{mix}}}{\partial \phi_i}\right). \tag{44}$$

Note that the energy barriers h_i mentioned in Eq. (41) are used to calculate the partial derivatives of the mixing energy f_{mix}, and for computing the Lagrange multiplier.

The general formulation for solving ϕ_i can be simplified in our case. First of all, the volume fraction of stainless steel ϕ_4 is defined based on a fixed configuration (Fig. 1):

$$\phi_4 = -\frac{1}{2}\tanh\left(\frac{|y - y_s| - d_s/2}{W}\right) + \frac{1}{2}, \tag{45}$$

where y_s is the center position of stainless steel in the y-axis, and d_s is the width. Second, the volume fraction of diamond grits ϕ_3 is also defined using a similar hyperbolic tangent function to outline the hexagonal shape, assumed a fixed configuration. Third, the volume fraction for filler metal ϕ_2 is solved at every time instant to reflect the wetting dynamics, and the volume fraction of argon gas is calculated by the constraint $\phi_1 = 1 - \sum_{i=2}^{4}\phi_i$. Finally, the Lagrange multiplier is updated from ϕ_1 to ϕ_4 at each time step.

E. Korteweg stress and momentum equation

During the phase transition process, the molten filler metal is assumed as a quasi-incompressible Newtonian fluid. The flow dynamics involved is described by the continuity equation and Navier–Stokes–Korteweg momentum equation as

$$\nabla \cdot \boldsymbol{v} = 0, \tag{46}$$

and

$$\rho\frac{D\boldsymbol{v}}{Dt} = \nabla\cdot\boldsymbol{\tau} - \nabla\cdot\sum_{i=1}^{4}\boldsymbol{\Pi}_i, \tag{47}$$

respectively, where ρ is the density that includes the contributions from all components,

$$\rho = \sum_{i=1}^{4}\phi_i\rho_i, \tag{48}$$

where ρ_1 to ρ_4 stand for the mass density of each component, $\boldsymbol{v}$ is the velocity field, $\boldsymbol{\tau}$ represents total viscous stress, and $\boldsymbol{\Pi}_i$ indicates the Korteweg stress introduced by capillarity effect across each interface. The constitutive stress-strain rate model for a Newtonian fluid can be formulated by

$$\boldsymbol{\tau} = -p\boldsymbol{\delta} + \boldsymbol{\sigma}_{\text{vis}} = -p\boldsymbol{\delta} + \eta\left[\nabla\boldsymbol{v} + (\nabla\boldsymbol{v})^T\right], \tag{49}$$

where p is pressure, $\boldsymbol{\delta}$ is the identity matrix, $\boldsymbol{\sigma}_{\text{vis}}$ is viscous stress, and η is a temperature-dependent dynamic viscosity, here calculated by

$$\eta = \phi_2\left[P\eta_2^{(\ell)} + (1-P)\eta_2^{(s)}\right] + \sum_{i=1,i\neq 2}^{4}\phi_i\eta_i, \tag{50}$$

with η_1, η_3, and η_4 representing the dynamic viscosity of argon gas, diamond grits, and stainless steel, $\eta_2^{(s)}$ and $\eta_2^{(\ell)}$ are the dynamics viscosity for solid and liquid filler metal, respectively, and P is the interpolation function defined by Eq. (13). Furthermore, using T_m as a reference temperature, the Korteweg stress according to the volume fraction can be derived[57] and expressed as

$$\boldsymbol{\Pi}_i = -T_m\xi_i^2\left(\frac{1}{2}|\nabla\phi_i|^2 + \phi_i\nabla^2\phi_i\right)\boldsymbol{\delta} + T_m\xi_i^2(\nabla\phi_i)(\nabla\phi_i), \tag{51}$$

where the isotropic part of the stress tensor above can be combined with the pressure effect in the momentum equation.

To facilitate the computation, the higher-order momentum equation can be reduced by introducing a potential form[58,59] through a free energy functional $\mathcal{F}$ and the corresponding non-classical chemical potential μ_i below:

$$\mathcal{F} = \int_\Omega\left[f(T,\varphi,\phi_1,\phi_2,\phi_3,\phi_4) + \frac{1}{2}T\xi_\varphi^2|\nabla\varphi|^2 + \frac{1}{2}\sum_{i=1}^{4}T\xi_i^2|\nabla\phi_i|^2\right]dV, \tag{52}$$

and

$$\mu_i = \frac{\delta\mathcal{F}}{\delta\phi_i} = \frac{\partial f}{\partial\phi_i} - T\xi_i^2\nabla^2\phi_i\,. \tag{53}$$

Here, we assume that the Korteweg effect is temperature independent and the reference temperature T_m is applied to the chemical potential. The body force term obtained from the Korteweg stress thus can be replaced by the free energy density and the chemical potential as

$$\nabla\cdot\sum_{i=1}^{4}\boldsymbol{\Pi}_i = \nabla\left(f - T_m\sum_{i=1}^{4}\xi_i^2\phi_i\nabla^2\phi_i\right) - \sum_{i=1}^{4}\mu_i\nabla\phi_i\,. \tag{54}$$

By absorbing the first term on the right-hand side of the above equation into the pressure gradient, the momentum equation can be simplified as

$$\rho\frac{D\boldsymbol{v}}{Dt} = -\nabla\hat{p} + \nabla\cdot\left[\eta(\nabla\boldsymbol{v} + \nabla\boldsymbol{v}^T)\right] + \sum_{i=1}^{4}\mu_i\nabla\phi_i, \tag{55}$$

where the modified pressure becomes

$$\hat{p} = p - \sum_{i=1}^{4}\left(T_m\xi_i^2\phi_i\nabla^2\phi_i\right) + f, \tag{56}$$

and the computation of chemical potential is separated from the momentum equation.

F. Material properties

As temperature variation is critical in thermal and momentum transport, we summarize the relevant properties and transport coefficients that take temperature dependency into account. The density of ideal argon gas is calculated by

$$\rho_1 = \frac{p_0 M_A}{RT}, \tag{57}$$

where p_0 is the ambient pressure, M_A is the molar mass of argon, R is the universal gas constant, and the data for thermal conductivity and dynamic viscosity[60] are correlated in terms of dimensional values in MKS units and degrees Kelvin as

$$k_{T_1} \simeq 1.473 \times 10^{-2} + 2.840 \times 10^{-5} T, \tag{58}$$

and

$$\eta_1 \simeq 1.885 \times 10^{-5} + 3.362 \times 10^{-8} T\,. \tag{59}$$

The above linear correlations are plotted against the temperature in Fig. 2(a) for reference.

A few material properties of commonly used nickel-based filler metals in brazing of diamond tools, such as BNi-2, BNi-3, and BNi-7 can be found in the literature.[18,61,62] However, these filler alloys, whether in solid or liquid form, are in general lack of temperature-dependent thermal physical properties. For the solid phase of the filler metal below melting temperature, we choose temperature-dependent thermal conductivity of a pure nickel[63] instead, whereas for the molten phase we adopt a constant conductivity from a liquid nickel at its melting temperature. Across the computational domain, we utilize the interpolation function P, Eq. (13), to determine the overall thermal conductivity as

$$k_{T_2} \simeq k_{Ni}^{(s)}[1 - P(\varphi)] + k_{Ni}^{(\ell)} P(\varphi), \tag{60}$$

and $k_{Ni}^{(s)}$ represents the solid-state thermal conductivity of pure nickel and is approximated by

$$k_{Ni}^{(s)} \simeq 50.06 + 0.022T, \tag{61}$$

where $k_{Ni}^{(\ell)} = 49.7\,\mathrm{W/(m \cdot K)}$ is the thermal conductivity of liquid nickel at its melting temperature.[64] The thermal conductivities of diamond[65] and stainless steel[66] can be estimated by

$$k_{T_3} \simeq 227.40 + 7.11 \times 10^6 T^{-1.53} \tag{62}$$

and

$$k_{T_4} \simeq 9.42 + 0.0143T, \tag{63}$$

respectively. These conductivities are plotted in Fig. 2(b). Other material properties used in the case studies are listed in Table I. A few more characteristic lengths and model parameters are included in Table II.

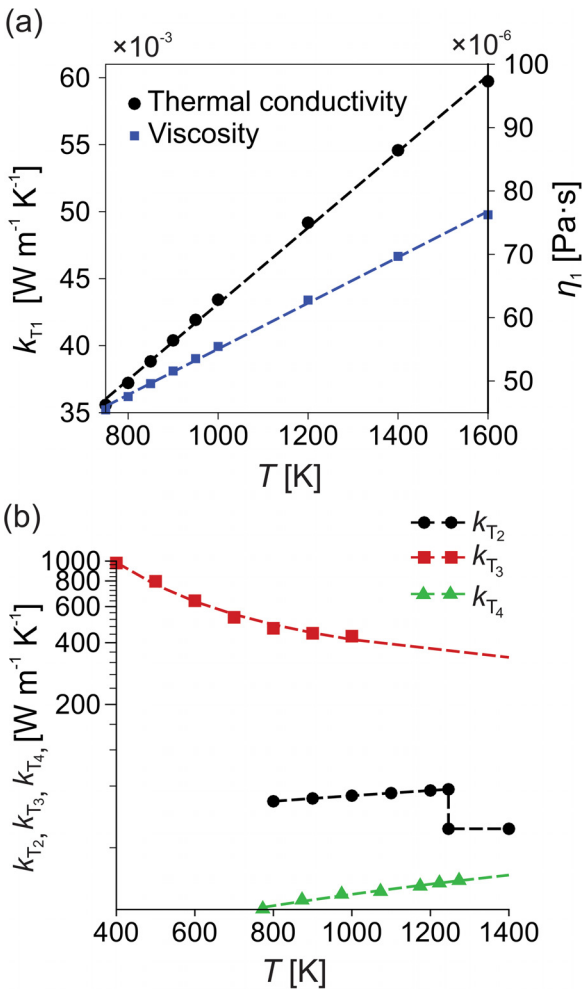

FIG. 2. (a) Temperature-dependent thermal conductivity k_{T_1}, and viscosity of argon gas η_1, (b) thermal conductivities of filler metal k_{T_2}, diamond grits k_{T_3}, and stainless steel substrate k_{T_4}.

G. Scaling and simplification

The governing equations (15), (34), (35), and (55) are scaled by the grit size L and phase transition timescale τ_φ (Table III). The scaling

TABLE I. Reference material properties.

Parameters	Value (SI)
Mass density:	$\mathrm{kg/m^3}$
Filler metal ρ_2[66]	7810
Diamond ρ_3[66]	3500
Stainless steel ρ_4[66]	7874
Reference thermal conductivity k_{T_0}[66]	$90.9\,\mathrm{W/(m \cdot K)}$
specific heat:	$\mathrm{J/(kg \cdot K)}$
Argon c_{p_1}[66]	520.3
Filler metal c_{p_2}[66]	490.0
Diamond c_{p_3}[69]	1994.2
Stainless steel c_{p_4}[66]	633.0
Liquid filler metal viscosity $\eta_2^{(\ell)}$[64]	$0.0125\,\mathrm{Pa \cdot s}$
Interfacial energy in between:	$\mathrm{J/m^2}$
Solid and liquid filler metal γ_φ[67]	0.347
Nickel and argon gas γ_{12}[66]	1.838
nickel and diamond γ_{23}[70]	2.572
Diamond and gas γ_{13}[70]	3.980
Stainless steel and argon gas γ_{14}[66]	1.860
Melting temperature of filler metal T_m[61]	1243 K
Latent heat of fusion of filler metal L_a[63]	$2.32 \times 10^9\,\mathrm{J/m^3}$
Emissivity:	
Filler metal ϵ_2[68]	0.34
Diamond grit ϵ_3[71]	0.20
Stainless steel ϵ_4[68]	0.40

TABLE II. Additional parameters used in test cases.

Parameters	Value (SI)
Grits size, characteristic length L	2×10^{-4} m
Domain size $D = 2\pi L$	$\sim 1.2 \times 10^{-3}$ m
Interfacial thickness for φ field W_φ	1.6×10^{-5} m
Interfacial thickness for ϕ_i field W	8×10^{-6} m
Temperature difference ΔT	500 K
Solid–liquid energy barrier h_φ	18.5 J/(m^3 · K)
Energy barrier for filler metal h_2	91.7 J/(m^3 · K)
Characteristic velocity U	0.73 m/s
Solid–liquid interfacial mobility M_φ	32.1 m · s · K/kg
2D power of laser beam $\mathcal{Q}$	2.1×10^5W/m
Spot size of laser beam a	100 μm
Scanning speed of laser beam U_a	0.1 m/s

and definition of reference parameters (with subscript 0) are based on filler metal as

$$\rho_0 = \rho_2, \quad c_{p_0} = c_{p_2}, \quad \text{and} \quad \eta_0 = \eta_2^{(\ell)}. \tag{64}$$

The characteristic velocity U is associated with the capillary velocity and adjusted by a constant β (here we select $\beta = 0.005$) as

$$U = \frac{\beta \gamma_{12}}{\eta_2^{(\ell)}}, \tag{65}$$

and the temperature is scaled by a characteristic temperature difference ΔT (assumed 500 K) as

$$\tilde{T} = \frac{T - T_m}{\Delta T}. \tag{66}$$

With the above reference parameters and material properties, five characteristic time scales involved in the SLB process can be determined, namely, thermal diffusion timescale τ_T, convective timescale τ_c, solid–liquid phase transition timescale τ_φ, the timescale for wetting dynamics τ_{wet}, and viscous diffusion timescale τ_{vis}, expressed as

$$\begin{aligned} &\tau_T = \frac{L^2 \rho_0 c_{p_0}}{k_{T_0}}, \quad \tau_c = \frac{L}{U}, \quad \tau_\varphi = \frac{1}{h_\varphi M_\varphi}, \\ &\tau_{\text{wet}} = \frac{L^2}{h_2 M_2}, \quad \text{and} \quad \tau_{\text{vis}} = \frac{\rho_0 L^2}{\eta_0}. \end{aligned} \tag{67}$$

The resulting values are listed in Table III. The pressure and stress involved in this problem are scaled by inertia effect $\rho_0 U^2$.

TABLE III. Time scales based on Eq. (67) and relevant parameters listed in Tables I and II.

Parameters	Value (s)
Thermal diffusion time τ_T	$\sim 1.68 \times 10^{-3}$
Convective timescale τ_c	2.74×10^{-4}
Phase transition timescale τ_φ	1.68×10^{-3}
Wetting dynamics timescale τ_{wet}	1.68×10^{-5}
Viscous diffusion time τ_{vis}	2.50×10^{-2}

Considering the scaling and reference parameters above, the energy equation can be simplified to a dimensionless form as

$$\begin{aligned} &\tilde{c}_p \left(\frac{\partial \tilde{T}}{\partial \tilde{t}} + \mathcal{P}_e \tilde{\boldsymbol{v}} \cdot \tilde{\nabla} \tilde{T} \right) + \frac{\phi_2 P'}{\mathcal{S}_{te}} \left(\frac{\partial \varphi}{\partial \tilde{t}} + \mathcal{P}_e \tilde{\boldsymbol{v}} \cdot \tilde{\nabla} \varphi \right) \\ &\quad = \mathcal{L}_{e_\varphi} \tilde{\nabla} \cdot \left(\tilde{k}_T \tilde{\nabla} \tilde{T} \right) + \mathcal{B}_r \mathcal{L}_{e_\varphi} \tilde{\boldsymbol{\sigma}}_{\text{vis}} : \tilde{\nabla} \tilde{\boldsymbol{v}} \\ &\qquad - \frac{\alpha \mathcal{B}_{i_{ir}} \mathcal{L}_{e_\varphi}}{\mathcal{C}_h \tilde{a}} \sqrt{\frac{2}{\pi}} \exp\left[\frac{-2(\tilde{x} - \tilde{x}_0 - \mathcal{P}e \tilde{U}_a \tilde{t})^2}{\tilde{a}^2} \right] (\hat{\boldsymbol{e}}_y \cdot \boldsymbol{n}) \\ &\qquad - \frac{\epsilon \mathcal{B}_{i_r} \mathcal{L}_{e_\varphi}}{\mathcal{C}_h} \left[\left(1 + \frac{\tilde{T} \Delta T}{T_m} \right)^4 - \left(1 + \frac{\tilde{T}_a \Delta T}{T_m} \right)^4 \right], \end{aligned} \tag{68}$$

where the tilde is used for scaled parameters, heat capacity $\tilde{c}_p = \sum_{i=1}^4 \phi_i \tilde{\rho}_i \tilde{c}_{p_i}$, thermal conductivity $\tilde{k}_T = \sum_{i=1}^4 \phi_i \tilde{k}_{T_i}$, emissivity $\epsilon = \sum_{i=1}^4 \phi_i \epsilon_i$, absorptivity is assumed the same as emissivity, $\alpha = \epsilon$, and the dimensionless groups are defined as

$$\begin{aligned} &\mathcal{P}_e = \frac{\tau_\varphi}{\tau_c}, \quad \mathcal{S}_{te} = \frac{\rho_0 c_{p_0} \Delta T}{L_a}, \quad \mathcal{L}_{e_\varphi} = \frac{\tau_\varphi}{\tau_T}, \\ &\mathcal{B}_r = \frac{\eta_0 U^2}{k_{T_0} \Delta T}, \quad \mathcal{B}_{i_r} = \frac{\sigma_B T_m^4 L}{k_{T_0} \Delta T}, \\ &\mathcal{B}_{i_{ir}} = \frac{\mathcal{Q}}{k_{T_0} \Delta T}, \quad \text{and} \quad \mathcal{C}_h = \frac{W}{L}. \end{aligned} \tag{69}$$

The Peclet number $\mathcal{P}_e$ compares the phase transition and convective time scales, Stefan number $\mathcal{S}_{te}$ measures the ratio of sensible heat to latent heat, interfacial Lewis number $\mathcal{L}_{e_\varphi}$ measures the ratio of the phase transition to thermal diffusion time scales, Brinkman number $\mathcal{B}_r$ compares the viscous dissipation to the heat conduction effects, Biot number $\mathcal{B}_{i_{ir}}$ measures the ratio of irradiation to heat conduction effect, Biot number $\mathcal{B}_{i_r}$ measures the radiation heat transfer to heat conduction effect, and $\mathcal{C}_h$ is the Cahn–Hilliard number indicating the relative thickness of the interface to the length scale. The scaled φ-equation can be expressed as

$$\begin{aligned} \frac{\partial \varphi}{\partial \tilde{t}} + \mathcal{P}_e \tilde{\boldsymbol{v}} \cdot \tilde{\nabla} \varphi &= \mathcal{C}_{h_\varphi}^2 \tilde{\nabla}^2 \varphi + \phi_2 (\varphi - \varphi^3) \\ &\quad + \phi_2 P' \Lambda_\varphi \frac{\tilde{T}}{1 + (\Delta T / T_m) \tilde{T}}, \end{aligned} \tag{70}$$

where an additional Cahn–Hilliard number $\mathcal{C}_{h_\varphi}$ represents the thickness of solid–liquid interface to the length scale, and the phase-change number Λ_φ describes the ratio of latent heat of fusion to the interfacial energy, defined as

$$\mathcal{C}_{h_\varphi} = \frac{W_\varphi}{L} \quad \text{and} \quad \Lambda_\varphi = \frac{L_a \Delta T}{h_\varphi T_m^2}, \tag{71}$$

respectively. Furthermore, the governing equation for the volume fraction of the filler metal ϕ_2 reduces to

$$\begin{aligned} &\frac{\partial \phi_2}{\partial \tilde{t}} + \mathcal{P}_e \tilde{\boldsymbol{v}} \cdot \tilde{\nabla} \phi_2 \\ &\quad = \frac{\tau_\varphi}{\tau_{\text{wet}}} \tilde{\nabla} \cdot \left\{ \tilde{\nabla} \left[\frac{\lambda}{h_2} - \mathcal{C}_h^2 \tilde{\nabla}^2 \phi_2 + 2\phi_2 (1 - \phi_2)(1 - 2\phi_2) \right] \right\}. \end{aligned} \tag{72}$$

Finally, the scaled Navier–Stokes–Korteweg momentum equation is written as

$$\frac{\tilde{\rho}}{\mathcal{S}_c}\left(\frac{\partial \tilde{\boldsymbol{v}}}{\partial t}+\mathcal{P}_e\,\tilde{\boldsymbol{v}}\cdot\tilde{\nabla}\tilde{\boldsymbol{v}}\right)\simeq-\mathcal{R}_e\nabla\tilde{p}+\mathcal{R}_e\Gamma\sum_{i=1}^{4}(\tilde{\mu}_i\tilde{\nabla}\phi_i)+\tilde{\nabla}\cdot\left[\tilde{\eta}(\tilde{\nabla}\tilde{\boldsymbol{v}}+\tilde{\nabla}\tilde{\boldsymbol{v}}^T)\right],\tag{73}$$

where the scaled chemical potential $\tilde{\mu}_i=\mu_i/(T_m h_2)$, density $\tilde{\rho}=\sum_{i=1}^{4}\phi_i\tilde{\rho}_i$, and the dynamic viscosity is

$$\tilde{\eta}=\phi_2\left[P\tilde{\eta}_2^{(\ell)}+(1-P)\tilde{\eta}_2^{(s)}\right]+\sum_{i=1,i\neq2}^{4}\phi_i\tilde{\eta}_i\,.\tag{74}$$

Note that the dynamic viscosities for all solid components are much larger than the dynamic viscosity of liquid filler metal; here, we assume $\tilde{\eta}_3=\tilde{\eta}_4=\tilde{\eta}_2^{(s)}\simeq10^5$. The Schmidt number $\mathcal{S}_c$ compares the phase transition to viscous time scales, Reynolds number $\mathcal{R}_e$ indicates the inertia to viscous effects, and Korteweg number Γ measures the ratio of energy barrier of filler metal to the kinetic energy, defined as

$$\mathcal{S}_c=\frac{\tau_\varphi}{\tau_{\text{vis}}},\quad \mathcal{R}_e=\frac{\tau_{\text{vis}}}{\tau_c},\quad \text{and}\quad \Gamma=\frac{T_m h_2}{\rho_0 U^2},\tag{75}$$

respectively. The dimensionless groups and their corresponding values are listed in Table IV for order-of-magnitude comparison.

In summary, the governing system and the assumptions are proposed to simulate the phase transition and wetting dynamics of diamond grits brazing process using nickel-based filler metal. Specifically, we solve energy equation [Eq. (15)] for the temperature distribution, solid liquid phase-field equation [Eq. (34)] for solid–liquid phase transition, volume fraction phase field equation [Eq. (35)] for wetting dynamics, and the Navier–Stokes–Korteweg equation [Eq. (55)] for fluid dynamics of the system. The fully coupled governing equations are solved with given initial and periodic boundary conditions. The computational algorithm is developed for the scaled formulation, and in general applicable to 2D and 3D cases.

III. RESULTS AND DISCUSSION

To demonstrate the transient dynamics, numerical tests are performed by applying an alternative spatial arrangement of the filler powders and diamond grits (Fig. 1). The results shown on the following figures are from discretization on a 2D mesh with 800×800 uniform grid points, and further refinement on the mesh will not generate the noticeable difference. A periodic boundary condition is applied to facilitate the computation using Fourier spectral method. The thermal conductivity of the substrate material has been adjusted to provide a quasi-insulation boundary condition at the bottom of the computational domain. The pseudo-spectral scheme is used to discretize nonlinear terms. The momentum equation is solved by using the projection formulation to decouple velocity field from the pressure field, and the solid phase is simply taken as an assumed fluid with much higher (at least five orders of magnitude) viscosity than the molten filler metal. The nonlinear effects induced by variable transport coefficients are discretized using the algorithm provided by Zhu *et al.*[72] The temporal discretization applies the forward Euler integration scheme with uniform time step $h=10^{-5}$, and a semi-implicit

TABLE IV. Dimensionless groups.

Dimensionless group	Value
Peclet number $\mathcal{P}_e$	6.14
Stefan number $\mathcal{S}_{te}$	0.82
Lewis number $\mathcal{L}_{e_\varphi}$	1
Brinkman number $\mathcal{B}_r$	1.47×10^{-7}
Biot number for radiation $\mathcal{B}_{i_r}$	5.96×10^{-4}
Biot number for irradiation $\mathcal{B}_{i_{ir}}$	0.018
Cahn–Hilliard number for φ field $\mathcal{C}_{h_\varphi}$	0.08
Phase change number Λ_φ	4.07×10^{4}
Cahn–Hilliard number for ϕ_i field $\mathcal{C}_h$	0.04
Reynold number $\mathcal{R}_e$	91.2
Schmidt number $\mathcal{S}_c$	0.067
Korteweg number Γ	27.4

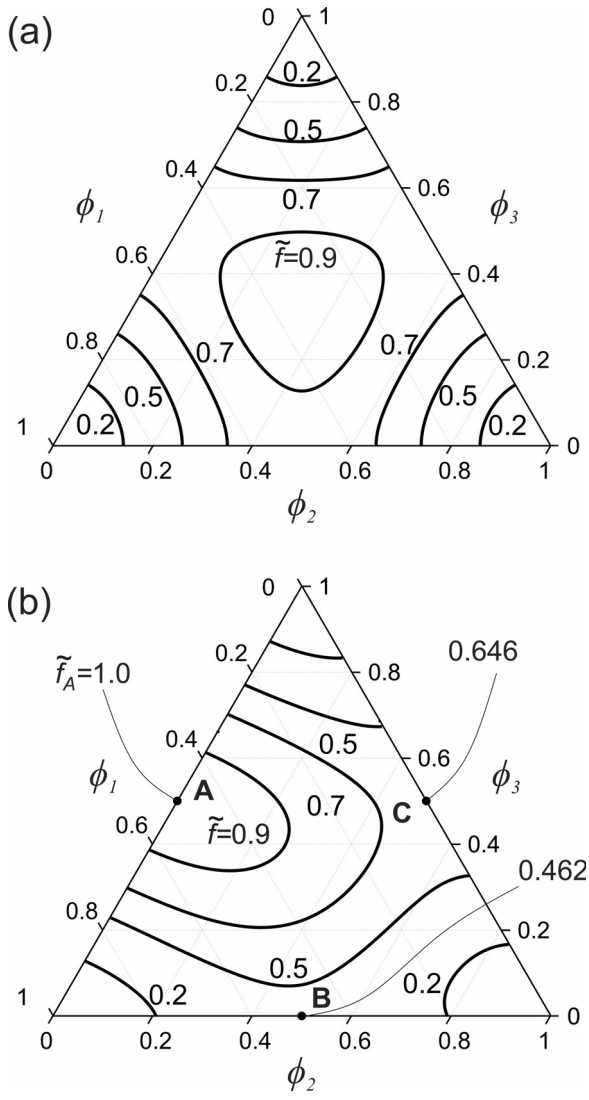

FIG. 3. Normalized free energy of an unbiased ternary system (a), and for an argon (ϕ_1)–filler metal (ϕ_2)–diamond (ϕ_3) system (b) at equilibrium.

spatial discretization is applied for all test cases. The transient simulations are carried out for about 5×10^5 time steps until the formation of meniscus around the diamond grits. Note that there is no smooth or adaptive scheme applied to the moving interfaces in the phase-field approach, which can be further extended to a variety of conditions with different powder size and configuration or spatial arrangement. Next, we present a validation of three-phase contact line dynamics and the simulation of SLB using stationary and moving laser beams.

A. Free energy of a ternary system

Figure 3 demonstrates the contour map of normalized free energy and its relation with the Young's contact angle under the steady-state condition for an assumed unbiased ternary system [Fig. 3(a)] and the argon-filler-diamond system [Fig. 3(b)], where the free energy f_{mix} [Eq. (31)] is scaled by its maximum value. For the unbiased case, $\gamma_{12} = \gamma_{13} = \gamma_{23}$, the energy barriers are based on a similar relationship as given in Eqs. (39) and (41), and the result indicates that the free energy has three locally minimum points at $(\phi_1, \phi_2, \phi_3) = (1, 0, 0)$, (0, 1, 0), and (0, 0, 1), implying a separation of the three-component system, which is equally weighted by a triple-well type energy potential with the global maximum located at the center point of the energy landscape, that is, $(\phi_1, \phi_2, \phi_3) = (1/3, 1/3, 1/3)$. On the other hand, for the argon-filler-diamond system, the energy barriers are calculated from interfacial energy γ_{12}, γ_{13}, and γ_{23} listed in Table II. The free energy has three local minima at the same locations as the unbiased system with a shifted global maximum. Points A($\phi_1 = 0.5$, $\phi_2 = 0$, $\phi_3 = 0.5$), B(0.5, 0.5, 0), and C(0, 0.5, 0.5) in Fig. 3(b) correspond to the interfaces between argon and diamond, argon and filler, and filler and diamond, respectively, with $\tilde{f}_A > \tilde{f}_C > \tilde{f}_B$, meaning that the system prefers to have a larger interfacial area between argon-filler or to reduce interface formation between argon and diamond. According to the definition of f_{mix} and interfacial energy relationship, Eq. (38), the free energy at points A–C can be correlated with interfacial free energy as $\tilde{f}_A : \tilde{f}_B : \tilde{f}_C = (h_1 + h_3) : (h_1 + h_2) : (h_2 + h_3) = \gamma_{13} : \gamma_{12} : \gamma_{23}$, which is associated with the steady-state Young's contact angle of a sessile droplet of liquid filler metal on top of a diamond plate in an argon gas environment by $\gamma_{13} - \gamma_{23} = \gamma_{12} \cos\theta$. The calculated contact angle is $\theta = \cos^{-1}[(\tilde{f}_A - \tilde{f}_C)/\tilde{f}_B] \simeq 40°$.

As a simple test of the steady-state model, wetting of the solid plate by a liquid droplet within a vapor environment under different contact angles is tested by evolving ϕ_2 equation from a spherical droplet to a fully relaxed state. The steady-state result shown in Fig. 4 at different contact angles agrees well with the theoretical profiles (dashed lines).

B. Brazing process using a stationary laser beam

Figure 5 demonstrates the transient dynamics of brazing of nickel-based filler metals using an assumed stationary laser beam with uniform irradiation intensity for the heating and melting process. To demonstrate the wetting process driven by interfacial energy alone, first, we neglect the convective effect in the process simulation. The 2D laser power $\mathcal{Q}$ is 2.1×10^5 W/m, spot radius $a \to \infty$, and the scanning speed is set to $U = 0$. The initial configuration at $\tilde{t} = 0$ is arranged by placing three powders of filler metals and three diamond grits of equal size and arranged alternatively on top of a layer of filler metal attached to the substrate (Fig. 1). Note that powder size $L = 200\ \mu$m and domain size $D \simeq 1200\ \mu$m. The process timescale τ_φ is about 1.7×10^{-3} s. The initial temperature $\tilde{T} = -0.2$ is uniform for all components including the argon gas environment. Figure 5 includes six sequential plots at scaled time instants $\tilde{t} = 0$, 0.5, 1.0, 1.3, 1.5, and 2.0. At each time instant, a color map on the left is for the phase field φ and side-by-side compared with a scaled temperature map $\tilde{T}$ on the right. The evolution of the filler metals and the configuration profiles

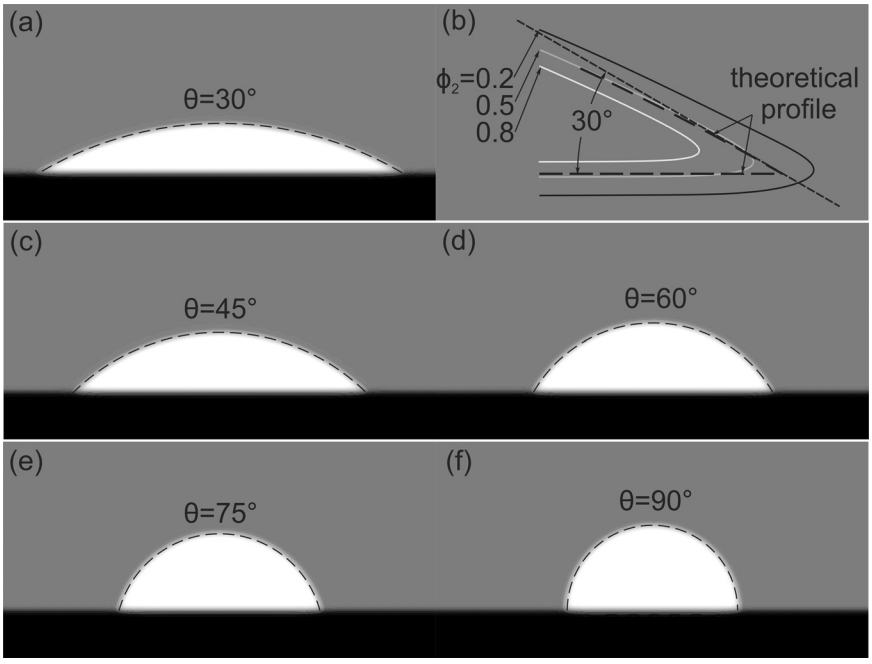

FIG. 4. A sessile liquid droplet on top of a solid substrate at different static contact angles. The gravity effect is neglected, and the theoretical profiles can be well approximated by a portion of a circle for $\theta = 30°$ (a), 45° (c), 60° (d), 75° (e), and 90° (f). The black area mimics the solid substrate (ϕ_3), the gray area is the for the vapor phase (ϕ_1), and the white area is the droplet (ϕ_2). The zoom-in view (b) shows phase-field contours at $\phi_2 = 0.2$, 0.5, and 0.8 near the tri-junction point, and the theoretical profile (long-dashed line) at a contact angle of 30°. Reference parameters: $T_m = 1243$ K, $W = 1 \times 10^{-6}$ m, $\gamma_{13} = 3.980$ J/m^2, $\gamma_{12} = 1.838$ J/m^2, and $\gamma_{23} = \gamma_{13} - \gamma_{12} \cos\theta$.

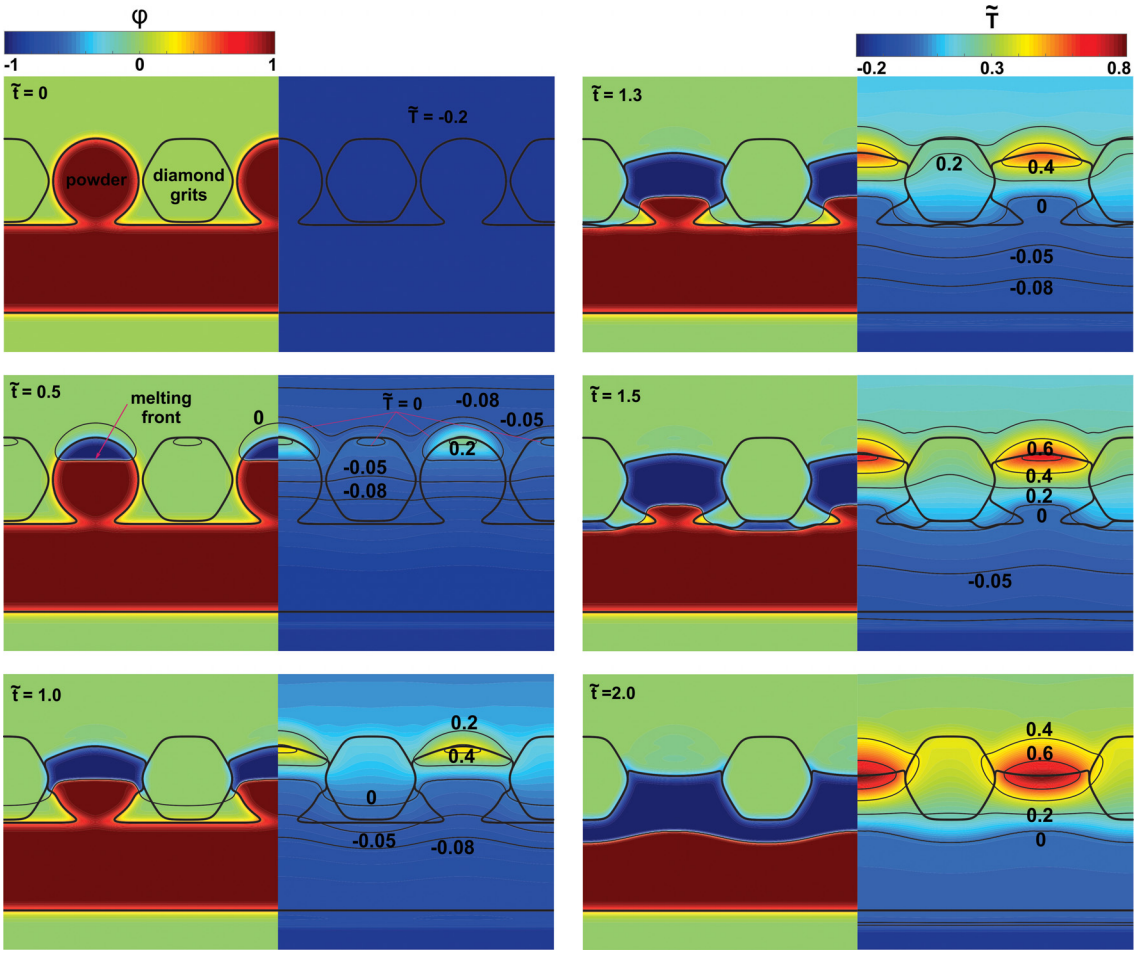

FIG. 5. Transient evolution of phase field φ for describing solid–liquid phase change and the scaled temperature field $\tilde{T}$ driven by heating from a laser beam with uniform intensity at six scaled time instants $\tilde{t}$=0, 0.5, 1.0, 1.3, 1.5, and 2.0. The sequential plots include temperature contours (thin solid lines) and boundary profiles of metals and diamond grits located at $\phi_2 = 0.5$ and $\phi_3 = 0.5$, respectively. The timescale is defined by $\tau_\varphi = 1.7 \times 10^{-3}$s, and the temperature is scaled as $\tilde{T} = (T - T_m)/(\Delta T)$, with melting temperature of the filler metal $T_m = 1243$ K and characteristic temperature difference $\Delta T = 500$ K.

of grits are indicated by thick solid lines determined by $\phi_2 = 0.5$ and $\phi_3 = 0.5$, whereas a few selected temperature contours are shown by thin solid lines for reference. In this case, the onset of melting appears at the top surface of the filler metal powders during the early stage of laser heating, shown at time instant around $\tilde{t} = 0.5$. At this moment, the filler powders are not in contact with diamond grits, and thus, a circular powder shape is maintained owing to a strong surface tension effect. The downward advancing of the melting front overlaps with the melting temperature contour $\tilde{T} = 0$, which validates the basic assumption that the process is thermally controlled and the solid–liquid interface is near an equilibrium state. The corresponding temperature map shows that the thermal diffusion wave has penetrated the filler metals and diamond grits at $\tilde{t} = 1.0$, as expected from scaling estimation. Furthermore, the evolution of the molten filler metals driven by wetting effect occurs at a later stage after time instant $\tilde{t}$ reaches about 1.0 (Fig. 5). The three-phase contact line moves upward and downward to coat the diamond grits, shown in the sequential plots at time instants $\tilde{t} = 1.0,\ 1.3$, and 1.5. During the process, higher temperature appears at the top surface of the filler powders due to higher absorptivity of thermal radiation ($\alpha \simeq 0.34$) compared to diamond grits ($\alpha \simeq 0.2$). At $\tilde{t} = 1.0$ and 1.3, one can observe a gradually deeper melting temperature contour appeared in the diamond grits compared with the filler metal. This is because of the absorption of latent heat into the filler metal in addition to its relatively low thermal conductivity [$k_{T_2} = 73.5$ vs $k_{T_3} = 281.6\,\mathrm{Wm^{-1}K^{-1}}$ at $T = T_m$, shown in Fig. 2(b)]. Eventually, the molten powders are fused with coated layer on the steel substrate, and the evolving interface fills the gap region as shown at $\tilde{t} = 2.0$. At this moment, a meniscus nearly at equilibrium is formed between diamond grits in order to provide the required bonding force. Continuous heating leads to further melting of the coated material.

In Fig. 6, we demonstrate the results by considering the convective effect using the same conditions for the case shown in Fig. 5. The two time instants at $\tilde{t} = 1.0$ and 2.0 are demonstrated with respect to the same time instants in Fig. 5. A symmetric circulation appears near the top interface of the filler powder due to the tendency of molten

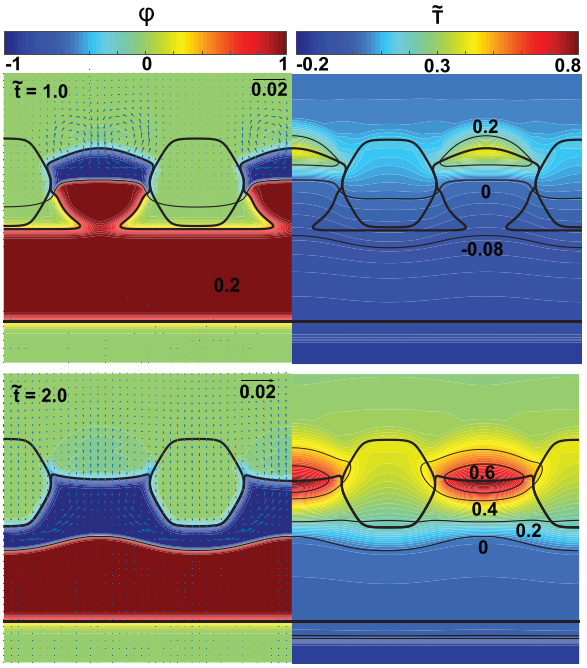

FIG. 6. Velocity field overlapped with phase and temperature fields for the case shown in Fig. 5. The magnitude of velocity vectors has been scaled by characteristic velocity $U = 0.73\,\mathrm{m/s}$.

filler metal to flatten the free surface on top and wet the diamond grits on the side. Comparing with Fig. 5, the overall interfacial morphology is very similar, indicating that the enhanced wetting due to convective or inertial effect is insignificant under a relatively low laser power. In this case, at around $\mathcal{Q} = 2.1 \times 10^5\,\mathrm{W/m}$. Away from the coating region of interest, the velocity vanishes in the far field as expected.

C. Brazing process using a scanning laser beam

Figure 7 shows the transient dynamics of the brazing process using an assumed Gaussian laser beam with the same laser power as the case shown in Fig. 5, $\mathcal{Q} = 2.1 \times 10^5\,\mathrm{W/m}$, and spot size $a = 100\,\mu\mathrm{m}$. Although under the same power, the peak value of the heat flux $\boldsymbol{H}$ from the scanning laser beam is about an order of magnitude higher than the case using a uniform heat flux $\boldsymbol{H}_u$. The scanning process starts from the left edge of the computational domain at $x_0 = 0$ and moves horizontally to the right-hand side with constant speed $u = 0.1\,\mathrm{m/s}$. The onset of the melting and wetting appears at the top-left corner around time instant $\tilde{t} = 0.5$, where the heating comes from thermal irradiation and heat conduction by direct contact of the filler metal with the diamond grit. The diamond grit has four times higher thermal conductivity and about two times higher thermal diffusivity than the nickel-based filler metal and thus overall resulting in a smaller temperature gradient (longer thermal diffusive length) in the diamond grits during the heating process. Note that the thermal diffusivities for argon gas, diamond grits, and filler metal are approximately 5.3×10^{-4}, 4.5×10^{-5}, and $2.1 \times 10^{-5}\,\mathrm{m^2/s}$. Further heating

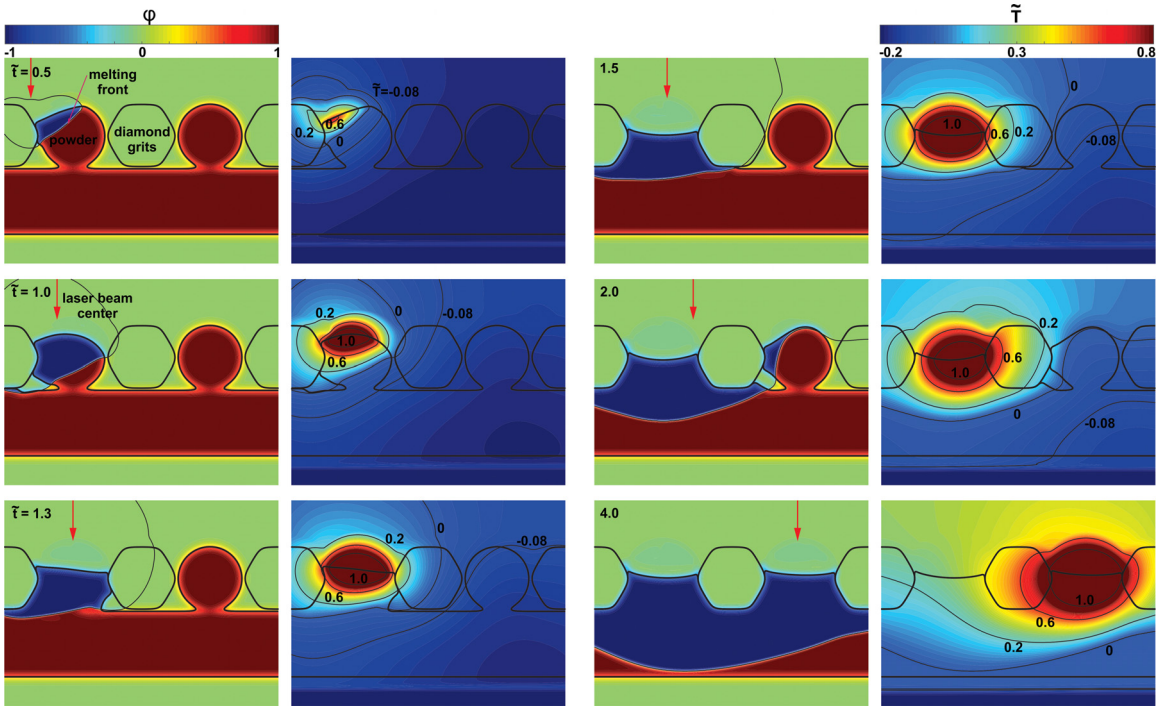

FIG. 7. Transient evolution of phase field φ and the scaled temperature field $\tilde{T}$ at six scaled time instants $\tilde{t} = 0.5$, 1.0, 1.3, 1.5, 2.0, and 4.0. The heating dynamics is driven by a scanning laser beam with 2D laser intensity $\mathcal{Q} = 2.1 \times 10^5\,\mathrm{W/m}$, spot size $a = 100\,\mu\mathrm{m}$, and scanning speed $u = 0.1\,\mathrm{m/s}$. The red arrow indicates the center position of the scanning laser beam.

from the scanning beam leads to an evolution of the melting front in the filler powder and the coated filler metal on the substrate. The three-phase contact line moves downward to coat the diamond grit at the left and then moves upward to coat the second diamond grit while filling the gap area ($\tilde{t} = 1.0$, 1.3, and 1.5). At time instant $\tilde{t} = 1.0$, the molten filler metal shifts to the left and the free surface maintains a circular shape due to strong surface tension effect. The sequential temperature plots clearly show the marching of the melting front at $\tilde{T} = 0$ and the accumulation and dissipation of the heat content. With continuous heating, the second filler powder melts and wets more grits ($\tilde{t} = 2.0$ and 4.0). The wetting dynamics eventually forms a meniscus between diamond grits.

Figure 8 demonstrates the temperature history of a few points in the diamond grits along with the liquid fraction of the filler metal during the transient process. As shown in Fig. 8(a), the process is driven by a stationary laser beam with uniform intensity. The temperature at three selected points within a diamond at the top, middle, and bottom places increases monotonically with first-order type profiles near the initial stage of heating. In the beginning, around $\tilde{t} \simeq 0.1$ the top surface reaches the melting temperature $\tilde{T}_m = 0$ so that fusion happens and the liquid fraction of the filler metal starts to increase (shown by the red dashed line). At around time $\tilde{t} \simeq 0.8$ to 0.9 heating and melting proceed along with capillary wetting, which fills the space, resulting in a slightly faster increase in temperature. This is due to the liquid filler coating on diamond grits, which causes higher laser energy absorption ($\alpha_2 \simeq 0.34$ vs $\alpha_3 \simeq 0.2$). In Fig. 8(b), we demonstrate a few more points to describe the temperature history around the diamond grits as well as the liquid fraction of the filler metal heated by a scanning laser beam. As expected, a strong ramp-up of temperature advances from left to right. Comparing with Fig. 8(a), a much higher temperature gradient and faster temperature rise appear on the surface of the diamond grit. This is due to the focused irradiation near the center point of a Gaussian beam. In the test case, the highest local heat flux is about an order of magnitude higher than the uniform beam. As the scanning proceeds to preheat the second and third diamond grits, at $\tilde{t} \simeq 1.0$, the surface temperature of first diamond grit (location 1) decreases due to less thermal irradiation and higher radiation heat loss to the gas environment, shown by temperature increase with a decayed magnitude. Meanwhile, the temperature at the bottom part of the grit continues to raise. The temperature history on location 3 closely correlates with the approaching and departing of the scanning laser beam. The heat conducted through the filler metal around the grit is influenced by the degree of wetting. At $\tilde{t} \simeq 2.8$, the highest temperature reaches $\tilde{T} \simeq 0.60$, which may cause degradation of the bonding strength due to possible graphitization of the diamond grits. On the other hand, once melting starts from the corner of the powder, the overall liquid fraction of the filler metal increases smoothly and correlates well to the increase in phase transition area. Comparing with the uniform heating case shown in Fig. 8(a), the demonstrated process using a scanning beam takes longer time ($\tilde{t} = 4.0$ vs $\tilde{t} = 2.0$) to complete. However, a larger molten zone is observed in the scanning case ($V_M = 68\%$ vs 37%).

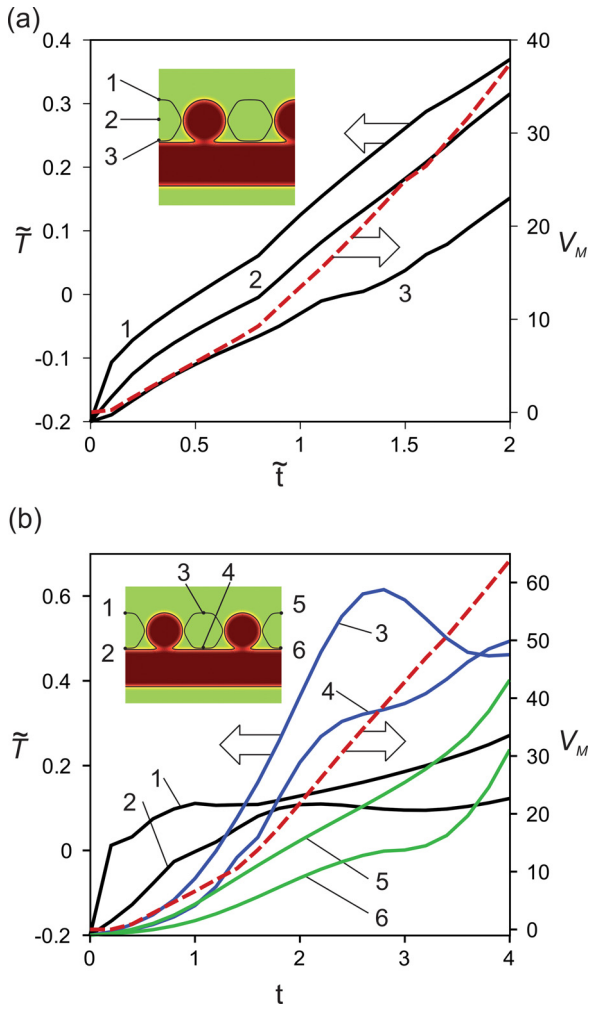

FIG. 8. Temperature history $\tilde{T}(\tilde{t})$ at a few selected points in diamond grits, and the liquid fraction of the overall filler metal V_m, either heated by a stationary (a) or scanning (b) laser beam.

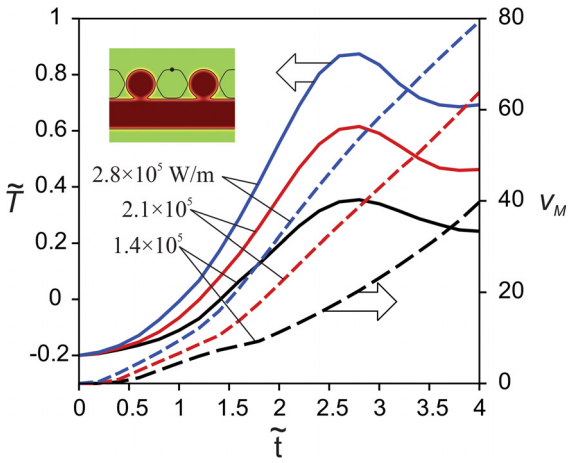

FIG. 9. Temperature history on the top surface of a diamond grit and the corresponding liquid fraction of the filler metal heated by a scanning laser beam with different thermal irradiation power.

Figure 9 demonstrates a sensitivity test of brazing dynamics based on different power of thermal irradiation. Applying the same configuration, initial and boundary conditions, and the traveling speed of the laser beam as shown in Fig. 8, with an increasing irradiation intensity H by adjusting the overall power Q. At a higher laser power, the brazing process completes faster but having a risk of overheating the diamond grits even within a short period of time. On the other hand, at lower power, the brazing process may not provide sufficient molten filler metal to bond the diamond grits completely.

IV. CONCLUSION

We present a thermodynamically consistent phase-field model to predict the dynamic process of selective laser brazing of diamond grits. The simplified 2D model features laser heating, melting, and wetting of nickel-based filler metal to diamond grits, as well as filling the voids and providing bonding to the grits. The phase-field framework has successfully incorporated the constraint of three-phase contact line dynamics with a non-isothermal phase transition process as well as the convective effect in the molten liquid metal. Computational results on heating efficiency and transient interfacial evolution under uniform and scanning laser beams are demonstrated. The temperature history, transient liquid fraction, and degree of completeness of the brazing process illustrate the potential of using the theoretical model to predict, design, and optimize the selective laser brazing process at a high level of precision. Future development of the laser brazing model will focus on experimental validation and thermal stress analysis with a different spatial arrangement and diamond protrusion height to facilitate the affinity or bonding strength and reduce graphitization of diamond grits to enhance cutting tool performance.

ACKNOWLEDGMENTS

L. Li and T.-H. Fan acknowledge the financial support of this research from the National Science Foundation (Grant No. CBET 1930906).

DATA AVAILABILITY

The data that support the findings of this study are available from the corresponding author upon reasonable request.

REFERENCES

[1]T. Takahashi and P. D. Funkenbusch, "Micromechanics of diamond composite tools during grinding of glass," Mater. Sci. Eng. A **285**(1–2), 69–79 (2000).
[2]W. Tillmann, "Trends and market perspectives for diamond tools in the construction industry," Int. J. Refract. Met. Hard Mater. **18**(6), 301–306 (2000).
[3]J. P. Davim, "Diamond tool performance in machining metal-matrix composites," J. Mater. Process. Technol. **128**(1–3), 100–105 (2002).
[4]Q. Bai, Y. Yao, and S. Chen, "Research and development of polycrystalline diamond woodworking tools," Int. J. Refract. Met. Hard Mater. **20**(5–6), 395–400 (2002).
[5]J. Konstanty, "Production of diamond sawblades for stone sawing applications," Key Eng. Mater. **250**, 1–12 (2003).
[6]A. Köpf, S. Feistritzer, and K. Udier, "Diamond coated cutting tools for machining of non-ferrous metals and fibre reinforced polymers," Int. J. Refract. Met. Hard Mater. **24**(5), 354–359 (2006).
[7]H. K. Tönshoff, H. Hillmann-Apmann, and J. Asche, "Diamond tools in stone and civil engineering industry: Cutting principles, wear and applications," Diam. Relat. Mater. **11**(3–6), 736–741 (2002).
[8]J. Konstanty, *Powder Metallurgy Diamond Tools* (Elsevier, Amsterdam, 2005).
[9]C. Artini, M. L. Muolo, and A. Passerone, "Diamond-metal interfaces in cutting tools: A review," J. Mater. Sci. **47**(7), 3252–3264 (2012).
[10]A. K. Chattopadhyay, L. Chollet, and H. E. Hintermann, "Experimental investigation on induction brazing of diamond with Ni–Cr hardfacing alloy under argon atmosphere," J. Mater. Sci. **26**(18), 5093–5100 (1991).
[11]S.-M. Chen and S.-T. Lin, "Brazing diamond grits onto a steel substrate using copper alloys as the filler metals," J. Mater. Eng. Perform. **5**(6), 761–766 (1996).
[12]S.-F. Huang, H.-L. Tsai, and S.-T. Lin, "Effects of brazing route and brazing alloy on the interfacial structure between diamond and bonding matrix," Mater. Chem. Phys. **84**(2–3), 251–258 (2004).
[13]C. H. Lee, J. O. Ham, M. S. Song, and C. H. Lee, "The interfacial reaction between diamond grit and Ni-based brazing filler metal," Mater. Trans. **48**(4), 889–891 (2007).
[14]Y. Chen, Y. Fu, H. Su, J. Xu, and H. Xu, "The effects of solder alloys on the morphologies and mechanical properties of brazed diamond grits," Int. J. Refract. Met. Hard Mater. **42**, 23–29 (2014).
[15]W. Qi, J. Lu, Y. Li, S. Xu, S. Zhong, B. Wang, and X. Qiu, "Vacuum brazing diamond grits with Cu-based or Ni-based filler metal," J. Mater. Eng. Perform. **26**(8), 4112–4120 (2017).
[16]M. F. Ismail, K. Yanagi, and H. Isobe, "Characterization of geometrical properties of electroplated diamond tools and estimation of its grinding performance," Wear **271**(3–4), 559–564 (2011).
[17]J. C. Sung and M. Sung, "The brazing of diamond," Int. J. Refract. Met. Hard Mater. **27**(2), 382–393 (2009).
[18]D. P. Sekulić, *Advances in Brazing: Science, Technology and Applications* (Elsevier, Amsterdam, 2013).
[19]S. Buhl, C. Leinenbach, R. Spolenak, and K. Wegener, "Microstructure, residual stresses and shear strength of diamond-steel-joints brazed with a Cu–Sn-based active filler alloy," Int. J. Refract. Met. Hard Mater. **30**(1), 16–24 (2012).
[20]A. B. Spierings, C. Leinenbach, C. Kenel, and K. Wegener, "Processing of metal-diamond-composites using selective laser melting," Rapid Prototyping J. **21**(2), 130–136 (2015).
[21]D. Rommel, F. Scherm, C. Kuttner, and U. Glatzel, "Laser cladding of diamond tools: Interfacial reactions of diamond and molten metal," Surf. Coat. Technol. **291**, 62–69 (2016).
[22]J. W. Cahn and J. E. Hilliard, "Free energy of a nonuniform system. I. Interfacial free energy," J. Chem. Phys. **28**(2), 258–267 (1958).
[23]J. W. Cahn, "On spinodal decomposition," Acta Metall. **9**(9), 795–801 (1961).
[24]O. Penrose and P. C. Fife, "Thermodynamically consistent models of phase-field type for the kinetics of phase transitions," Phys. D **43**(1), 44–62 (1990).
[25]S.-L. Wang, R. F. Sekerka, A. A. Wheeler, B. T. Murray, S. R. Coriell, R. J. Braun, and G. B. McFadden, "Thermodynamically-consistent phase-field models for solidification," Phys. D **69**(1–2), 189–200 (1993).
[26]D. M. Anderson, G. B. McFadden, and A. A. Wheeler, "Diffuse-interface methods in fluid mechanics," Annu. Rev. Fluid Mech. **30**(1), 139–165 (1998).
[27]R. F. Sekerka, "Irreversible thermodynamic basis of phase field models," Philos. Mag. **91**(1), 3–23 (2011).
[28]R. Kobayashi, "Modeling and numerical simulations of dendritic crystal growth," Phys. D **63**(3–4), 410–423 (1993).
[29]A. A. Wheeler, B. T. Murray, and R. J. Schaefer, "Computation of dendrites using a phase field model," Phys. D **66**, 243–262 (1993).
[30]J. A. Warren and W. J. Boettinger, "Prediction of dendritic growth and microsegregation patterns in a binary alloy using the phase-field method," Acta Metall. Mater. **43**(2), 689–703 (1995).
[31]B. T. Murray, A. A. Wheeler, and M. E. Glicksman, "Simulations of experimentally observed dendritic growth behavior using a phase-field model," J. Cryst. Growth **154**, 386–400 (1995).
[32]A. Karma and W.-J. Rappel, "Quantitative phase-field modeling of dendritic growth in two and three dimensions," Phys. Rev. E **57**(4), 4323–4349 (1998).
[33]W. J. Boettinger, J. A. Warren, C. Beckermann, and A. Karma, "Phase-field simulation of solidification," Annu. Rev. Mater. Res. **32**, 163–194 (2002).
[34]J.-L. Liu, Z.-X. Nie, and W.-G. Jiang, "Deformation field on the soft substrate induced by capillary force," Phys. B **404**, 1195–1199 (2009).
[35]J.-L. Liu and R. Xia, "A unified analysis of a micro-beam, droplet and CNT ring adhered on a substrate: Calculation of variation with movable boundaries," Acta Mech. Sin. **29**(1), 62–72 (2013).

[36]P. K. Mondal, U. Ghosh, A. Bandopadhyay, D. DasGupta, and S. Chakraborty, "Electric-field-driven contact-line dynamics of two immiscible fluids over chemically patterned surfaces in narrow confinements," Phys. Rev. E **88**, 023022 (2013).
[37]P. K. Mondal, D. DasGupta, and S. Chakraborty, "Interfacial dynamics of two immiscible fluids in spatially periodic porous media: The role of substrate wettability," Phys. Rev. E **90**, 013003 (2014).
[38]P. K. Mondal, U. Ghosh, A. Bandopadhyay, D. DasGupta, and S. Chakraborty, "Pulsating electric field modulated contact line dynamics of immiscible binary systems in narrow confinements under an electrical double layer phenomenon," Soft Matter **10**, 8512–8523 (2014).
[39]P. K. Mondal, D. DasGupta, A. Bandopadhyay, and S. Chakraborty, "Pulsating flow driven alteration in moving contact-line dynamics on surfaces with patterned wettability gradients," J. Appl. Phys. **116**, 084302 (2014).
[40]P. K. Mondal, D. DasGupta, and S. Chakraborty, "Rheology-modulated contact line dynamics of an immiscible binary system under electrical double layer phenomena," Soft Matter **11**, 6692–6702 (2015).
[41]G. Kunti, P. K. Mondal, A. Bhattacharya, and S. Chakraborty, "Electrothermally modulated contact line dynamics of a binary fluid in a patterned fluidic environment," Phys. Fluids **30**, 092005 (2018).
[42]Z.-H. Shen, J.-J. Wang, J.-Y. Jiang, S. X. Huang, Y.-H. Lin, C. W. Nan, L.-Q. Chen, and Y. Shen, "Phase field modeling and machine learning of electric–thermal–mechanical breakdown of polymer-based dielectrics," Nat. Commun. **10**, 1–10 (2019).
[43]Q. Wang, G. Zhang, Y. Li, Z. Hong, D. Wang, and S. Shi, "Application of phase-field method in rechargeable batteries," npj Comput. Mater. **6**, 1–8 (2020).
[44]P. Bazazi, A. Sanati-Nezhad, and S. H. Hejazi, "Wetting dynamics in two-liquid systems: Effect of the surrounding phase viscosity," Phys. Rev. E **97**, 063104 (2018).
[45]T.-W. Zhang, J. Wu, and X.-J. Lin, "An interface-compressed interface method and its application for multiphase flow," Phys. Fluids **31**, 122102 (2019).
[46]J.-Q. Li, T.-H. Fan, T. Taniguchi, and B. Zhang, "Phase-field modeling on laser melting of a metallic powder," Int. J. Heat Mass Transfer **117**, 412–424 (2018).
[47]J.-Q. Li and T.-H. Fan, "Phase-field modeling of metallic powder-substrate interaction in laser melting process," Int. J. Heat Mass Transfer **133**, 872–884 (2019).
[48]T.-H. Fan, J.-Q. Li, B. Minatovicz, E. Soha, L. Sun, S. Patel, B. Chaudhuri, and R. Bogner, "Phase-field modeling of freeze concentration of protein solutions," Polymers **11**(1), 10 (2018).
[49]J.-Q. Li and T.-H. Fan, "Phase-field modeling of macroscopic freezing dynamics in a cylindrical vessel," Int. J. Heat Mass Transfer **156**, 119915 (2020).
[50]W. Villanueva, W. J. Boettinger, J. A. Warren, and G. Amberg, "Effect of phase change and solute diffusion on spreading on a dissolving substrate," Acta Mater. **57**(20), 6022–6036 (2009).
[51]H. Ding and P. D. M. Spelt, "Wetting condition in diffuse interface simulations of contact line motion," Phys. Rev. E **75**(4), 046708 (2007).
[52]A. Fakhari and D. Bolster, "Diffuse interface modeling of three-phase contact line dynamics on curved boundaries: A lattice Boltzmann model for large density and viscosity ratios," J. Comput. Phys. **334**, 620–638 (2017).
[53]H.-R. Liu, P. Gao, and H. Ding, "Fluid-structure interaction involving dynamic wetting: 2D modeling and simulation," J. Comput. Phys. **348**, 45–65 (2017).
[54]F. Boyer and C. Lapuerta, "Study of a three component Cahn–Hilliard flow model," ESAIM: Math. Modell. Numer. Anal. **40**(4), 653–687 (2006).
[55]F. Boyer and S. Minjeaud, "Numerical schemes for a three component Cahn–Hilliard model," ESAIM: Math. Modell. Numer. Anal. **45**(4), 697–738 (2011).
[56]J. M. Park and P. D. Anderson, "Diffuse-interface modeling of three-phase interactions," Appl. Phys. Lett. **108**(19), 191604 (2016).
[57]A. Onuki, *Phase Transition Dynamics* (Cambridge University Press, Cambridge, 2004).
[58]D. Jacqmin, "Calculation of two-phase Naiver–Stokes flows using phase-field modeling," J. Comput. Phys. **155**(1), 96–127 (1999).
[59]A. G. Lamorgese, D. Molin, and R. Mauri, "Phase field approach to multiphase flow modeling," Milan J. Math. **79**(2), 597–642 (2011).
[60]E. Vogel, B. Jäger, R. Hellmann, and E. Bich, "*Ab initio* pair potential energy curve for the argon atom pair and thermophysical properties for the dilute argon gas. II. Thermophysical properties for low-density argon," Mol. Phys. **108**(24), 3335–3352 (2010).
[61]AWS, *A5.8/A5.8M. Specification for Filler Metals for Brazing and Braze Welding* (AWS, Florida, 2004).
[62]AWS, *Brazing Handbook* (AWS, Florida, 2004).
[63]*CRC Materials Science and Engineering Handbook*, 4th ed., edited by J. F. Shackelford (CRC Press, Boca Raton, 2016).
[64]M. F. Arenas, V. L. Acoff, and R. G. Reddy, "Physical properties of selected brazing filler metals," Sci. Technol. Weld. Joining **9**(5), 423–429 (2004).
[65]J. Guo, B. Wen, R. Melnik, S. Yao, and T. Li, "Geometry and temperature dependent thermal conductivity of diamond nanowires: A non-equilibrium molecular dynamics study," Phys. E **43**(1), 155–160 (2010).
[66]*CRC Handbook of Chemistry and Physics*, edited by W. M. Haynes (CRC Press, Boca Raton, 2012).
[67]H. Jones, "The solid–liquid interfacial energy of metals: Calculations versus measurements," Mater. Lett. **53**, 364–366 (2002).
[68]*Smithells Metals Reference Book*, edited by W. F. Gale and T. C. Totemeier (Elsevier, Amsterdam, 2004).
[69]H. O. Pierson, *Handbook of Carbon, Graphite, Diamond and Fullerenes* (Noyes, Park Ridge, 1993).
[70]N. Eustathopoulos, M. G. Nicholas, and B. Drevet, *Wettability at High Temperatures* (Elsevier, Amsterdam, 1999).
[71]C. R. Lin, D. H. Wei, C. K. Chang, and W. H. Liao, "Optical properties of diamond-like carbon films for antireflection coating by RF magnetron sputtering method," Phys. Procedia **18**, 46–50 (2011).
[72]J. Zhu, L.-Q. Li, J. Shen, and V. Tikare, "Coarsening kinetics from a variable-mobility Cahn–Hilliard equation: Application of a semi-implicit Fourier spectral method," Phys. Rev. E **60**(4), 3564–3572 (1999).